

Spin bath mediated long-lived coherent oscillations of NV centers in diamond

Akshat Rana,¹ Pooja Lamba,¹ Basanta Mistri,² Dieter Suter,³
Siddharth Dhomkar,^{2,4,5,*} and Rama K. Kamineni^{1,6,†}

¹*Department of Physics, Bennett University, Greater Noida 201310, India*

²*Department of Physics, IIT Madras, Chennai 600036, India*

³*Fakultät Physik, Technische Universität Dortmund, D-44221 Dortmund, Germany*

⁴*Center For Quantum Information, Communication And Computing, IIT Madras, Chennai 600036, India*

⁵*London center for Nanotechnology, UCL, London WC1H0AH, UK*

⁶*SIAS, Krea University, Sri City 517646, India*

(Dated: June 30, 2026)

Decoherence is the biggest bottleneck in all quantum technologies. For nitrogen-vacancy (NV) centers in diamond, the loss of coherence is caused by the electron and nuclear spin bath of the diamond lattice. Here, we demonstrate that the spin bath - that typically causes decoherence - entangles the spin states of the NV electron and the host ^{14}N nucleus. The many-body interaction between the ^{14}N nucleus - electron - bath spins at an energy level anti-crossing occurring for an applied magnetic field orientation perpendicular to the NV axis is responsible for this effect. This is observed experimentally on NV ensembles via electron spin-echo measurements, where the echo envelope is modulated at the frequency of a ^{14}N nuclear spin transition. Using numerical simulations, we show that the spin bath coupling to the NV centers is essential for observing this modulation. Due to the zero first-order Zeeman effect at the anti-crossing, the observed oscillations have long spin-echo coherence times, 2–3 times those at the parallel magnetic field orientation. The oscillation frequency is highly stable and robust against environmental fluctuations. These findings provide new opportunities for fundamental studies of many-body physics and quantum sensing.

Long coherence times are one of the fundamental prerequisites of quantum technologies [1, 2]. For fault-tolerant quantum computing, coherence times of the qubits must be much longer than the gate operation times, typically by several orders of magnitude [3, 4]. Quantum networks based on repeaters require high-fidelity and long-lived memories for storing and synchronizing quantum information [5, 6]. In quantum sensing, the sensitivity of the probing qubit depends on its ability to maintain superposition states for a long duration [7, 8].

Optical spin initialization and readout combined with long coherence times and miniature sensor size make NV centers in diamond useful for several quantum technologies including quantum information processing and metrology [9–11]. Decoherence of NV centers is caused by the electron spins of paramagnetic impurities and the ^{13}C nuclear spins of the diamond lattice [12]. In ultra-pure diamond crystals containing low concentration of paramagnetic impurities, the spin bath is dominated by ^{13}C nuclear spins [13]. The coherence time of NV centers can be extended by applying dynamical decoupling pulse sequences [14, 15]. This coherence time depends on the angle between the NV-axis and the direction of the applied static magnetic field. It has been reported that the coherence time of NV centers in ultra-pure diamond crystals is maximum when the field is aligned with the NV axis [16, 17]. In diamond crystals containing very high concentration of paramagnetic impurities, it is

shown that the coherence time improves if the field is oriented perpendicular to the NV axis [18]. However, in these crystals, the coherence time is only a few microseconds, limiting their applications.

The simplest of the dynamical-decoupling pulse sequences is the spin-echo sequence, which employs a π -pulse at the center of the free-evolution period [19]. When the spin bath is dominated by ^{13}C nuclear spins, the electron spin-echo signal shows characteristic decays and revivals at one-half of the ^{13}C Larmor precession frequency [20]. The decay in the amplitude of the revivals is characterized as the T_2 coherence time of the NV centers. The spin-1 character of the NV electron spin and the anisotropic nature of the hyperfine interaction with the ^{13}C spins (spin-1/2) are crucial for understanding the echo revivals. The quantization axis of the bath nuclear spins depends on the state of the NV electron spin. Due to this, the spin states of the bath nuclei are conditioned on the electron spin state. When the electron spin is prepared in a superposition state, the resulting entanglement between the electron spin and the bath nuclear spins leads to decoherence of the signal. Decoupling of the spin bath occurs when one-half of the free-evolution time is equal to an integral multiple of the ^{13}C Larmor precession period, leading to the revival of the echo signal. The strongly coupled ^{13}C nuclear spins proximal to the NV center cause electron spin-echo envelope modulations (ESEEM) [20].

The host ^{14}N atom of the NV center possesses a spin-1 nucleus with a strong nuclear quadrupolar coupling, whose principal axis coincides with the NV-axis. Since the ^{14}N atom is positioned on the NV axis, its hyperfine tensor is axially symmetric. The Zeeman interaction of

* sdholmkar@physics.iitm.ac.in

† koti.kamineni@gmail.com

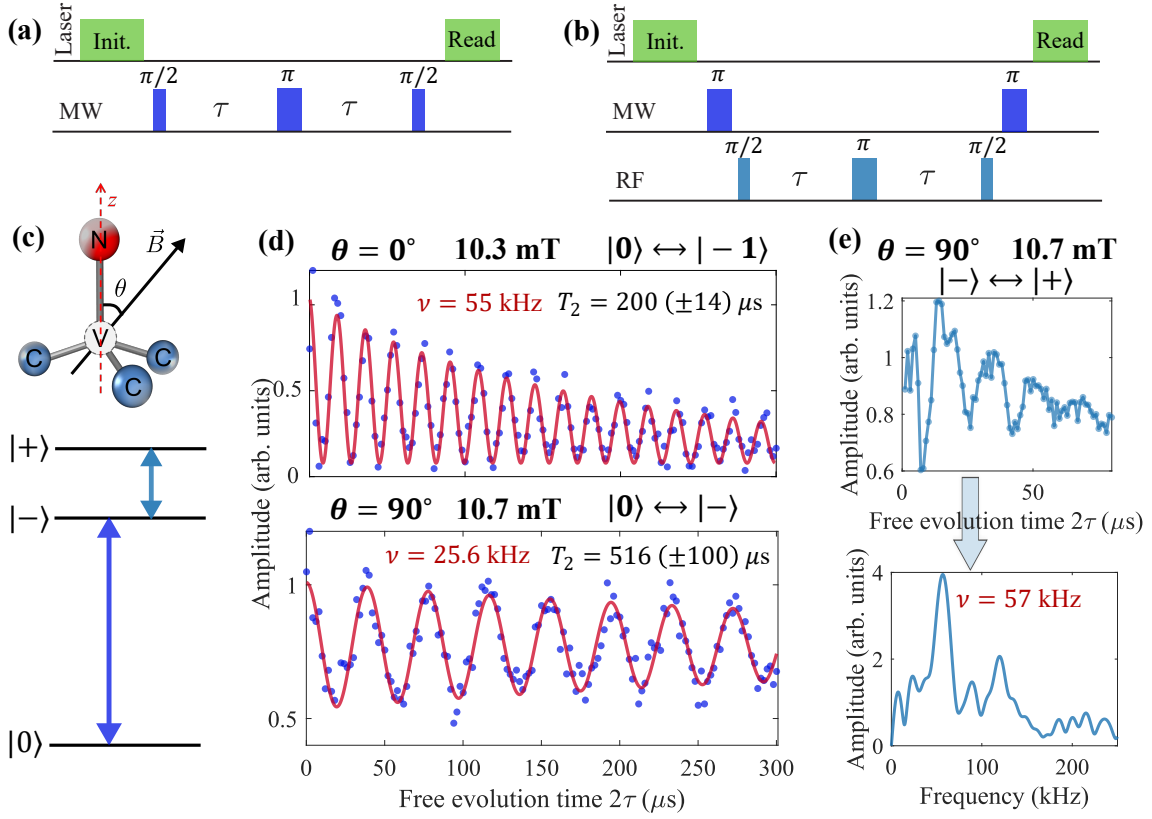


FIG. 1. Pulse sequences for electron spin-echo measurements: (a) for the transitions $|0\rangle \leftrightarrow |-1\rangle$ and $|0\rangle \leftrightarrow |- \rangle$, and (b) for $|- \rangle \leftrightarrow |+ \rangle$. (c) Schematic of the NV center along with the magnetic field vector, and the electron spin energy levels at $\theta = 90^\circ$. (d) Spin-echo signals measured on ensemble NV centers for the transitions $|0\rangle \leftrightarrow |-1\rangle$ and $|0\rangle \leftrightarrow |- \rangle$. The data for the transition $|0\rangle \leftrightarrow |-1\rangle$ are fitted to the expression $a \cos^2(\pi\nu 2\tau) \exp[-(2\tau/T_2)^n] + b$ with $n \approx 1$, and the data for $|0\rangle \leftrightarrow |- \rangle$ are fitted to $a \cos(2\pi\nu 2\tau) \exp(-2\tau/T_2) + b$. (e) Spin-echo signal and its Fourier transform for the electron spin transition $|- \rangle \leftrightarrow |+ \rangle$, whose frequency is 32 MHz for a transverse magnetic field strength of 10.7 mT.

the ^{14}N nuclear spin is typically small compared to the quadrupolar coupling. When a static magnetic field is applied parallel to the NV-axis, the quantization axes of both electron and ^{14}N nuclear spins align with the NV-axis. Consequently, the nuclear spin eigenbasis is common to all the electron spin manifolds. Here, we observe that the ^{14}N nuclear spin state is conditioned on the NV electron spin state when a magnetic field in the range 6–21 mT is applied perpendicular to the NV-axis. Interestingly, this occurs due to the hyperfine coupling between the electron spin and the bath ^{13}C nuclear spins, in particular, due to the off-diagonal elements of the hyperfine tensor. As a characteristic of this ^{14}N nucleus - electron - ^{13}C spin bath many-body interaction, the electron spin-echo signal is modulated by a ^{14}N nuclear spin transition, whose frequency depends on the quadrupolar interaction, the transverse ^{14}N hyperfine parameter, and the magnetic field. These electron spin-echo modulations also have long coherence times, 2–3 times the T_2 values at the parallel field, due to the zero first-order Zeeman (ZEFOZ) shift occurring at the energy level anti-crossings induced by the transverse field.

The Hamiltonian of the ground-state of the NV center

in an applied magnetic field can be written as

$$\mathcal{H}_1 = DS_z^2 - \gamma_e \vec{B} \cdot \vec{S}, \quad (1)$$

where $\vec{B} = B(\sin\theta \cos\phi, \sin\theta \sin\phi, \cos\theta)$ and $\vec{S} = (S_x, S_y, S_z)$ are the magnetic field and spin-1 angular momentum vectors respectively. Here, we set $\hbar = 1$ and use frequency units for energy. $D = 2870$ MHz and $\gamma_e = -28025$ MHz/T are the zero-field splitting parameter and gyromagnetic ratio of the electron spin respectively. When the magnetic field is applied parallel to the NV axis, the eigenstates of the electron spin can be written as $|0\rangle$, $|-1\rangle$, and $|1\rangle$, where 0, -1, 1 are the eigenvalues of the S_z operator. When the field is applied perpendicular to the NV axis, the energy level anti-crossing [21, 22] causes strong mixing between the $|-1\rangle$ and $|1\rangle$ states, and the eigenstates can be approximately written as $|0\rangle$, $|- \rangle$, and $|+ \rangle$, where $|\pm \rangle = \frac{|-1\rangle \pm |1\rangle}{\sqrt{2}}$.

We perform electron spin-echo measurements on two diamond crystals containing NV center ensembles, where the spin bath is dominated by ^{13}C nuclear spins. Fig. 1(a) shows the pulse sequence used to drive the transitions $|0\rangle \leftrightarrow |-1\rangle$ at $\theta = 0^\circ$ and $|0\rangle \leftrightarrow |- \rangle$ at $\theta = 90^\circ$.

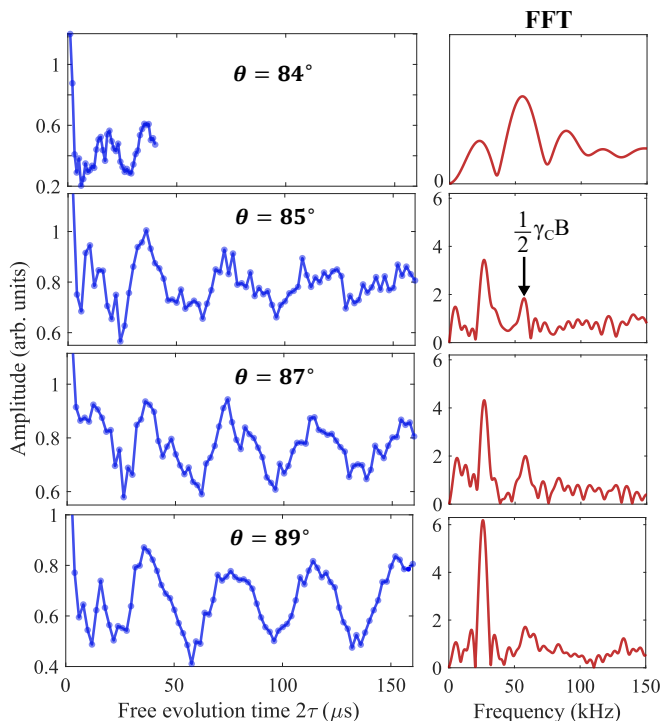


FIG. 2. Time-domain spin-echo signals and their Fourier transforms (FFTs) for magnetic field orientations orthogonal to the NV-axis. Here, $B = 10.7$ mT.

The corresponding results, obtained at magnetic field strengths of 10.3 and 10.7 mT respectively, are shown in Fig. 1(d). For the parallel field, the signal shows characteristic decays and revivals at one-half of the ^{13}C Larmor precession frequency ($\frac{1}{2}\gamma_C B$, where γ_C is the gyromagnetic ratio of the ^{13}C nuclear spin). The T_2 coherence time is measured to be $208 (\pm 13) \mu\text{s}$. For the transverse field and the $|0\rangle \leftrightarrow |-\rangle$ transition, the signal shows oscillations with a T_2 value of $516 (\pm 100) \mu\text{s}$. Importantly, the frequency of the oscillations is 25.6 kHz, which is quite different from the $\frac{1}{2}\gamma_C B = 57$ kHz. Similar oscillations are observed for the $|0\rangle \leftrightarrow |+\rangle$ transition as well.

For the transverse field, the transition between the states $|-\rangle$ and $|+\rangle$ is allowed as illustrated in Fig. 1(c). The spin-echo signal of this transition is also measured by using the pulse sequence shown in Fig. 1(b). Since optical pumping does not directly create a population difference between the states $|-\rangle$ and $|+\rangle$, microwave (MW) π -pulses on resonance with the transition $|0\rangle \leftrightarrow |-\rangle$ are used to transfer population from the $|0\rangle$ state to the $|-\rangle$ state and back (for readout). The radio-frequency (RF) pulses, shown in the third row of Fig. 1(b), are applied on resonance with the electron spin transition $|-\rangle \leftrightarrow |+\rangle$, whose transition frequency is 32 MHz. The resulting spin-echo signal along with its Fourier transform are shown in Fig. 1(e). It shows decays and revivals at $\frac{1}{2}\gamma_C B = 57$ kHz, but the coherence time is significantly shorter compared to the other transitions. The presence of 25.6 kHz ESEEM oscillations (at 10.7

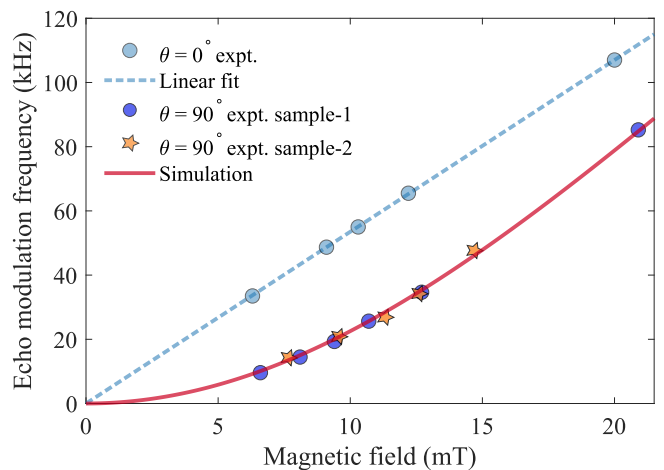


FIG. 3. Frequencies of spin-echo modulations as a function of the magnetic field strength for parallel ($\theta = 0^\circ$) and transverse ($\theta = 90^\circ$) directions with respect to the NV axis. $\theta = 0^\circ$ data follow $\frac{1}{2}\gamma_C B$, whereas $\theta = 90^\circ$ data are fitted to a ^{14}N transition frequency ($|e^-, ^{14}\text{N}, ^{13}\text{C}\rangle = |0, +, \alpha_1\rangle \leftrightarrow |0, -, \alpha_1\rangle$, where $|\pm\rangle = \frac{|-1\rangle \pm |1\rangle}{\sqrt{2}}$ and $|\alpha_1\rangle$ is a superposition of $|-\frac{1}{2}\rangle$ and $|\frac{1}{2}\rangle$). Error bars for the modulation frequencies are smaller than the data-point markers.

mT) for the transitions $|0\rangle \leftrightarrow |-\rangle$ and $|0\rangle \leftrightarrow |+\rangle$, and their absence for the transition $|-\rangle \leftrightarrow |+\rangle$ indicates that the transition responsible for these modulations must be in the $|0\rangle$ subspace.

To understand these oscillations further, we measure spin-echo signals for a range of θ values near the transverse field orientation. The resulting signals and their Fourier transforms are shown in Fig. 2. At $\theta = 84^\circ$, the signal decays very quickly and it shows very weak modulation associated with ^{13}C Larmor precession. As θ increases to 85° , the 25.6 kHz ESEEM oscillations start to appear. The amplitude of these oscillations and their coherence time increase as θ approaches 90° , while the modulation associated with ^{13}C Larmor precession becomes negligible. This indicates that both enhanced T_2 and ESEEM oscillations originate due to the transverse magnetic field. Note that the frequency of oscillations isn't changing with the direction of the applied magnetic field.

The echo modulation frequency as a function of the magnetic field strength for both parallel and transverse orientations are shown in Fig. 3. As expected, the echo revival frequencies for $\theta = 0^\circ$ can be fitted to $\frac{1}{2}\gamma_C B$. However, the ESEEM frequency at $\theta = 90^\circ$ increases non-linearly with the field strength.

When a magnetic field is applied perpendicular to the NV-axis, the expectation values of the electron spin angular momentum operators, $\langle S_x \rangle = \langle S_y \rangle = \langle S_z \rangle = 0$, for all the three approximate eigenstates $|0\rangle$ and $|\pm\rangle$. The energy levels become insensitive to the Zeeman and hyperfine interactions in the first-order [23, 24]. This is known as ZEFOZ shift [25]. The effect of the spin bath on the

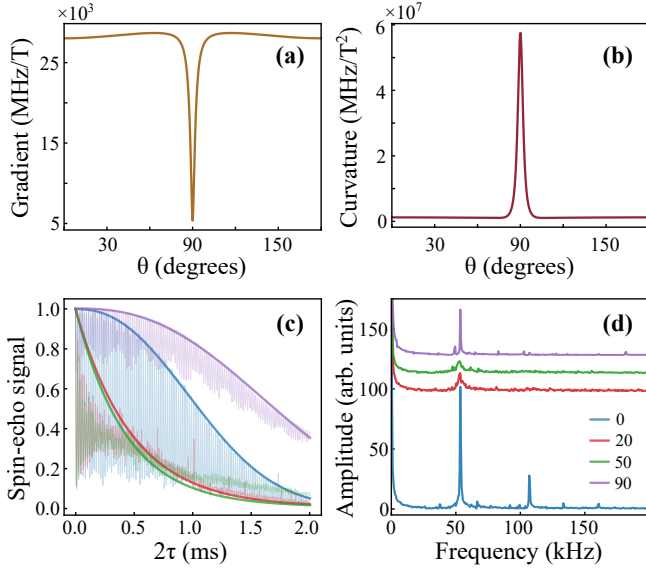


FIG. 4. (a) and (b) Calculated gradient and curvature of an electron spin transition frequency with respect to magnetic field noise as a function of the polar angle (θ) of the static field at $B = 10$ mT. (c) and (d) CCE-2 spin-echo simulation results of the electron spin transition $|0\rangle \leftrightarrow |-1\rangle$ (or $|-\rangle$) for different values of θ and their Fourier transforms (FFTs). The FFT traces have been shifted vertically for better visibility. The T_2 values are 1.2, 0.5, 0.4, and 2.0 ms for $\theta = 0^\circ, 20^\circ, 50^\circ$, and 90° respectively.

NV electron spin can be seen as a fluctuating magnetic noise that shifts the transition frequencies. However, at ZEFOZ points, the gradient of the transition frequencies with respect to the magnetic field is strongly suppressed. Due to this, spin systems tend to have long coherence times at ZEFOZ points [25–27].

For parallel field, the gradient of the transition frequencies with respect to magnetic field is equal to γ_e . At transverse field, it is approximately equal to $2\gamma_e^2 B/D$ (Supplementary Section S4). Though the gradient is not exactly zero here, it is significantly lower for field strengths satisfying $\gamma_e B \ll D$. As the first-order magnetic-field sensitivity is suppressed, the contribution of second-order magnetic-field fluctuations to decoherence becomes more significant. This effect can be quantified by the curvature (second derivative) of the transition frequencies with respect to the magnetic field [28]. Gradient and curvature of the $|0\rangle \leftrightarrow |-1\rangle$ transition as a function of θ are shown in Figs. 4(a) and (b). The gradient decreases sharply at $\theta = 90^\circ$, while the curvature increases rapidly. Though the curvature is high at $\theta = 90^\circ$, its contribution to decoherence is orders of magnitude smaller than that of the gradient. Hence, we expect an improvement in T_2 for a transverse field.

In order to quantify the dependence of coherence time on θ , the spin-bath dynamics are modeled using the cluster correlation expansion (CCE) method, which approximates the many-body evolution of the nuclear environment by decomposing it into contributions from finite

clusters of spins [29, 30] (Methods). The results, plotted in Figs. 4(c) and (d), show that T_2 decreases significantly as the angle between the magnetic field and the NV axis increases. However, it increases again for a transverse field, reaching its maximum value at $\theta = 90^\circ$, where it is close to twice the value obtained at $\theta = 0^\circ$, in accordance with the experimental observations. Nevertheless, at $\theta = 90^\circ$, the CCE-2 simulations do not reproduce the ESEEM modulations observed in the experiment. Instead, they show low-amplitude modulations with a frequency of $\frac{1}{2}\gamma_C B$. The nuclear spin of the host ^{14}N atom has been excluded in the CCE-2 simulations, and it appears that the observed modulation frequency is related to it.

The ESEEM oscillations observed in the experiment at the transverse field can be explained by using a 3-spin system containing the NV electron spin, ^{14}N nuclear spin, and a ^{13}C nuclear spin of the bath. The corresponding Hamiltonian of the system can be written as

$$\begin{aligned} \mathcal{H}_2 = & DS_z^2 - \gamma_e \vec{B} \cdot \vec{S} + A_{\parallel}^N S_z I_z^N + A_{\perp}^N (S_x I_x^N + S_y I_y^N) \\ & + P(I_z^N)^2 - \gamma_N \vec{B} \cdot \vec{I}^N + \vec{S} \cdot \mathbf{A}^C \cdot \vec{I}^C - \gamma_C \vec{B} \cdot \vec{I}^C, \end{aligned} \quad (2)$$

where A_{\parallel}^N and A_{\perp}^N are the parallel and perpendicular components of the ^{14}N hyperfine interaction. $P = -4.95$ MHz and $\gamma_N = 3.08$ MHz/T are the quadrupole coupling and gyromagnetic ratio of the ^{14}N nuclear spin respectively. \mathbf{A}^C represents the hyperfine tensor of the ^{13}C nuclear spin. Using this Hamiltonian, we simulate the electron spin-echo signal of the $|0\rangle \leftrightarrow |-1\rangle$ transition (Methods). It involves a total of twelve energy levels. However, the main features of the echo signal can be explained by using a set of four energy levels, two each from the $|0\rangle$ and $|-1\rangle$ subspaces. These are shown in Fig. 5. The eigenstates are ordered as $|e^-, ^{14}\text{N}, ^{13}\text{C}\rangle$. For the ^{14}N nucleus, $|\pm\rangle = \frac{|-1\rangle \pm |1\rangle}{\sqrt{2}}$ and for ^{13}C , $|\pm\rangle = \frac{1}{\sqrt{2}}(|-\frac{1}{2}\rangle \pm |\frac{1}{2}\rangle)$. The complete energy level diagram is given in Supplementary Section S2.

The term $A_{zx}^C S_z I_x$ of the ^{13}C hyperfine interaction is crucial in explaining the experimental echo modulations. Here z and x refer to the NV-axis and the direction of the magnetic field perpendicular to the NV-axis respectively. The energy level diagram for the case $\theta = 90^\circ$ and $A_{zx}^C = 0$ is shown in Fig. 5(a). Here, the nuclear spin states are independent of the electron spin state. The allowed electron spin transitions are $|0, +, +\rangle \leftrightarrow |-1, +, +\rangle$ and $|0, -, +\rangle \leftrightarrow |-1, -, +\rangle$. The first $\pi/2$ pulse of the spin-echo sequence excites these transitions, however, it does not create any coherence in the nuclear spin sublevels. Correspondingly, the spin-echo signal does not show any modulations. The energy level diagram for $A_{zx}^C = 0.25$ MHz is shown in Fig. 5(b). Here, if the electron spin state is $|0\rangle$, the spin states of the ^{14}N nucleus are $|\pm\rangle$, and if the electron spin state is $|-1\rangle$, the ^{14}N spin states are $|\pm 1\rangle$, i.e., the ^{14}N nuclear spin state is conditioned on the electron spin state because of an off-diagonal ele-

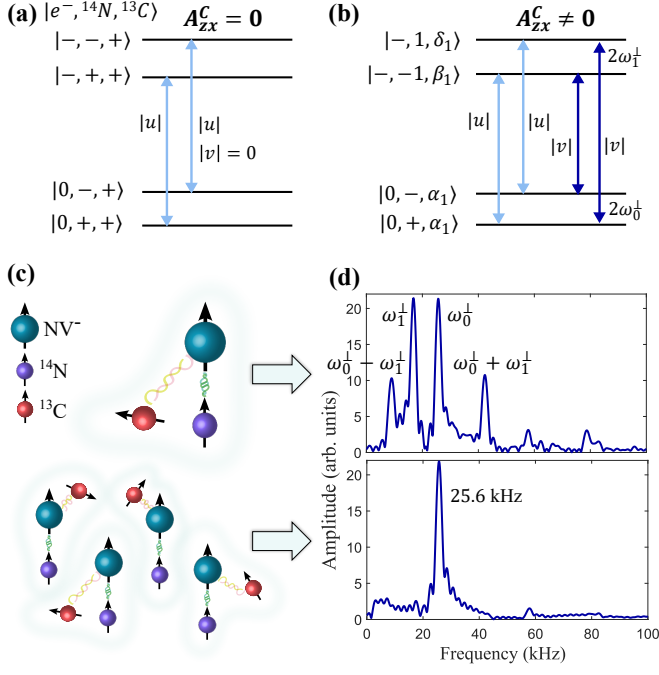


FIG. 5. Electron spin-echo simulations of a ^{14}N nuclear - NV electron - ^{13}C nuclear spin system in a transverse magnetic field. Relevant energy level diagram for (a) the ^{13}C hyperfine parameter $A_{zx}^C = 0$ and (b) $A_{zx}^C = 0.25$ MHz. (c) Schematic of the spin system. (d) Fourier transforms of the simulated spin-echo signals at 10.7 mT. The upper spectrum is simulated with the ^{13}C hyperfine parameters $A_{xx}^C = 0.17$, $A_{yy}^C = 0.08$, $A_{zz}^C = 0.13$, $A_{xy}^C = 0.10$, $A_{zx}^C = 0.25$, and $A_{zy}^C = 0.05$ MHz. The lower spectrum is obtained by averaging over 11 different ^{13}C hyperfine couplings strengths in the range 0.05-0.25 MHz. For electron and ^{14}N nuclear spins $|\pm\rangle = \frac{|-1\rangle \pm |1\rangle}{\sqrt{2}}$, for ^{13}C $|\pm\rangle = \frac{1}{\sqrt{2}}(|-\frac{1}{2}\rangle \pm |\frac{1}{2}\rangle)$, and $|\alpha_1\rangle \approx 0.81|\frac{1}{2}\rangle + 0.58|-\frac{1}{2}\rangle$, $|\beta_1\rangle \approx 0.74|\frac{1}{2}\rangle + 0.66|-\frac{1}{2}\rangle$, $|\delta_1\rangle \approx 0.63|\frac{1}{2}\rangle + 0.78|-\frac{1}{2}\rangle$ for $A_{zx}^C = 0.25$.

ment of the ^{13}C hyperfine tensor. All the four electron spin transitions between the energy levels are allowed. The $\pi/2$ -pulse of the spin-echo sequence simultaneously excites all the four transitions, and it leads to creation of the nuclear spin coherences $|0, +, \alpha_1\rangle \leftrightarrow |0, -, \alpha_1\rangle$ and $|-, -1, \beta_1\rangle \leftrightarrow |-, 1, \delta_1\rangle$. In this scenario, the spin-echo signal is expected to be modulated at the transition frequencies of these two transitions, and also at their sum and difference frequencies. It can be expressed as [31]

$$\mathcal{S}(t) = |u|^4 + |v|^4 + |u|^2|v|^2[2\cos(\omega_0^\perp t) + 2\cos(\omega_1^\perp t) - \cos((\omega_0^\perp - \omega_1^\perp)t) - \cos((\omega_0^\perp + \omega_1^\perp)t)], \quad (3)$$

where $|u|$ and $|v|$ represent the amplitudes of the electron spin transitions, and $2\omega_0^\perp$ and $2\omega_1^\perp$ are equal to the frequency differences of the nuclear spin sublevels corresponding to different electron spin states as shown in Fig. 5(b).

The Fourier transformed spectrum of the simulated spin-echo signal for a transverse field of amplitude 10.7

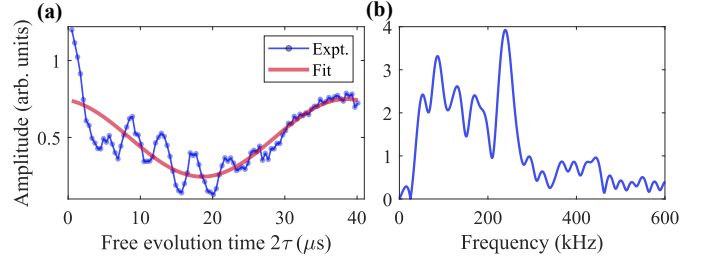


FIG. 6. (a) High-resolution electron spin-echo signal of the $|0\rangle \leftrightarrow |-\rangle$ transition in a transverse magnetic field of 10.7 mT and (b) its Fourier transform. The 25.6 kHz oscillation shown by red curve in (a) is subtracted before the Fourier transformation.

mT and $A_{zx}^C = 0.25$ MHz is shown in Fig. 5(d) (upper trace). The peak frequencies and their relative amplitudes are in excellent agreement with Eq. 3. The frequency ω_0^\perp depends on the values of A_\perp^N , P , and B , where as the frequency ω_1^\perp depends on the values of A_\parallel^N , A_{zx}^C , and B . Since, ω_1^\perp depends on the value of A_{zx}^C , the peaks corresponding to ω_1^\perp , $\omega_0^\perp - \omega_1^\perp$, and $\omega_0^\perp + \omega_1^\perp$ average out when averaged over different ^{13}C hyperfine coupling strengths (0.05 - 0.25 MHz) as shown in the lower trace of Fig. 5(d). ω_0^\perp , which is equal to one-half of the ^{14}N transition frequency $|0, +, \alpha_1\rangle \leftrightarrow |0, -, \alpha_1\rangle$, does not depend on ^{13}C hyperfine parameters. Correspondingly the peak at ω_0^\perp survives the averaging. Its frequency (25.6 kHz) exactly matches the experimental ESEEM frequency at 10.7 mT for $P = -4.95$ MHz and $A_\perp^N = -2.64$ MHz. Furthermore, the plot of ω_0^\perp as a function of B in Fig. 3 fits very well with all the measured modulation frequencies. Simulations show that the electron spin-echo signal is modulated by ω_0^\perp if at least one ^{13}C nuclear spin is coupled to the NV center with $A_{zx}^C > 0.01$ MHz. The spin-echo modulation at ω_0^\perp occurs even when multiple ^{13}C nuclear spins are coupled to the NV center. The results of a simulation consisting of three ^{13}C nuclear spins coupled to an NV center are shown in Supplementary Section S3.

The frequency of the observed spin-echo modulation (ω_0^\perp) is a result of the second-order interactions at the transverse magnetic field, involving the ^{14}N nuclear spin parameters P and A_\perp^N . These parameters have low sensitivity to temperature and strain compared to the NV electron spin parameters D and E [32–34]. Hence, the modulation frequency should be robust against strain and thermal fluctuations. The slope of the modulation frequency with respect to the transverse magnetic field at 10 mT is 4.44 MHz/T, which is much smaller than the typical electron spin gradient $\gamma_e = 28025$ MHz/T. The long coherence times of the modulations can partly compensate their low sensitivity to magnetic fields. Overall, the observed ESEEM frequency is highly stable and inherently robust against environmental variations.

A high-resolution spin-echo signal of the $|0\rangle \leftrightarrow |-\rangle$ transition, measured at $\theta = 90^\circ$ is shown in Fig. 6.

It shows small amplitude, high-frequency modulations, whose Fourier transform shows multiple peaks in the frequency range 60-250 kHz. Simulations suggest that these frequencies could be due to strongly coupled ^{13}C nuclear spins (Supplementary Section S3). They may be more clearly observable in experiments with single NV centers. These modulations in single NV centers can be used to characterize ^{13}C hyperfine interactions. Furthermore, the simulations indicate that these additional modulations are highly sensitive to off-axis (non-transverse) magnetic fields, which may be useful for magnetometry.

In conclusion, we have demonstrated spin-bath mediated, long-lived electron spin-echo envelope modulations of NV centers in diamond in transverse magnetic fields. The long coherence times can be attributed to the ZEF shift at the energy level anti-crossing point induced by the transverse field. The modulation frequency belongs to a nuclear spin transition of the host ^{14}N atom. However, the electron spin-echo envelope is modulated by this frequency because of the ^{13}C nuclear spin bath coupling to the electron spin. The many-body interaction between the ^{14}N nuclear, electron, and ^{13}C bath nuclear spins is crucial for explaining the result. This work opens new directions for understanding the role of quantum many-body interactions in solid-state spin systems. Although demonstrated here using the NV-center platform in diamond, the underlying mechanism is expected to arise in similar solid-state defect spin systems coupled to nuclear spin baths, e.g., NV centers in silicon carbide.

METHODS

Samples: Two chemical vapor deposition grown single crystal diamond samples of dimensions $3 \times 3 \times 0.5$ mm and $2 \times 2 \times 1$ mm are used in this work. Their nitrogen concentration is about 1 ppm and they contain natural abundance of ^{13}C atoms.

Experimental setup: All the experiments of this work have been performed on a home-built confocal microscope setup equipped with microwave and radio-frequency electronics for the resonant excitation of the electron spins of NV centers. A 532 nm diode pumped solid-state laser is used to initialize and readout the electron spins. A single-photon detector based on an avalanche photo-diode is used to measure the fluorescence of NV centers. A 560 nm long-pass dichroic mirror separates the laser and fluorescence beam paths. The laser light, reflected by the dichroic mirror, is focused onto the diamond crystal by using an objective lens having 1.45 NA. The fluorescence emitted by the NV centers is collected by the same objective lens and it gets transmitted through the dichroic mirror. A 50 μm pinhole is used in the detection path to filter the out of plane fluorescence. The lateral and axial resolutions of the confocal spot are about 0.25 and 1 μm respectively. From the nitrogen concentration of the diamond crystal and the photoluminescence intensity, we can estimate that there

are hundreds of NV centers in the confocal volume. Static magnetic field is applied to NV centers by using a permanent magnet. The orientation of the static field with respect to the diamond crystal is controlled by using two rotation stages connected to the magnet.

CCE-simulation: Here, we consider that the central NV electron spin ($S = 1$) is interacting with a surrounding bath of ^{13}C ($I = 1/2$) nuclear spins. The ^{13}C spin bath is generated by randomly occupying sites of the diamond lattice according to the natural isotopic abundance ($\sim 1.1\%$). Interactions between the NV electronic spin and the nuclear spins are modeled using the purely dipolar hyperfine tensor. For each realization, the bath radius is fixed to 3 nm, while the maximum separation between correlated ^{13}C pairs included in the calculation is restricted to 0.5 nm. These parameters resulted in bath realizations containing approximately 220 individual ^{13}C spins and about 100 coupled ^{13}C pairs. The Hahn-echo coherence signal is evaluated within the CCE-2 approximation by including both single-spin and pair-cluster contributions. To account for statistical variations in the spin environment and, thus, to mimic ensemble effects, the simulations are averaged over 20 independent bath realizations, and the resulting averaged coherence is presented in Fig. 4(c). The detailed CCE workflow is as follows.

For a given magnetic field, the NV electron spin Hamiltonian is diagonalized and the two lowest-energy eigenstates are selected to define an effective qubit. The spin operators are projected onto this dressed-state subspace according to

$$\tilde{S}_\alpha = PS_\alpha P, \quad (4)$$

where P is the projector onto the chosen two-level subspace.

The hyperfine interaction tensor between the NV electron spin and the i th ^{13}C nuclear spin is approximated by the magnetic dipole-dipole interaction,

$$A_{i,\alpha\beta} = \frac{\mu_0 \gamma_e \gamma_C \hbar}{4\pi r_i^3} (\delta_{\alpha\beta} - 3\hat{r}_{i,\alpha}\hat{r}_{i,\beta}), \quad \alpha, \beta \in \{x, y, z\}, \quad (5)$$

where $r_i = |\vec{r}_i|$ is the distance between the NV center and the i th nucleus, $\hat{r}_i = \vec{r}_i/r_i$ is the corresponding unit vector, $\hat{r}_{i,\alpha}$ denotes its α th Cartesian component, and $\delta_{\alpha\beta}$ is the Kronecker delta.

Let $\{|0\rangle, |1\rangle\}$ denote the two dressed NV qubit states. The effective Hamiltonian of a single nuclear spin conditioned on the NV qubit state $m \in \{0, 1\}$ is

$$H_i^{(m)} = \gamma_C \vec{B} \cdot \vec{I}_i + \sum_{\alpha,\beta} \langle m | \tilde{S}_\alpha | m \rangle A_{i,\alpha\beta} I_{i,\beta}. \quad (6)$$

To incorporate pairwise bath correlations, pairs of ^{13}C nuclei separated by less than 0.5 nm are retained. The

effective Hamiltonian of a nuclear-spin pair (i, j) is

$$H_{ij}^{(m)} = H_i^{(m)} + H_j^{(m)} + H_{ij}^{\text{dip}}, \quad (7)$$

where the nuclear dipolar interaction is

$$H_{ij}^{\text{dip}} = \frac{\mu_0 \gamma_C^2 \hbar}{4\pi r_{ij}^3} \left[\vec{I}_i \cdot \vec{I}_j - 3(\vec{I}_i \cdot \hat{r}_{ij})(\vec{I}_j \cdot \hat{r}_{ij}) \right]. \quad (8)$$

Hahn Echo Evolution: For each cluster, the conditional propagators associated with the two dressed NV qubit states are

$$U_C^{(m)}(\tau) = e^{-iH_C^{(m)}\tau}, \quad (9)$$

where $m \in 0, 1$ labels the two dressed NV qubit states. The coherence contribution of a cluster is calculated as

$$L_C(2\tau) = \text{Tr} \left[U_C^{(1)\dagger} U_C^{(0)\dagger} U_C^{(1)} U_C^{(0)} \rho_C \right], \quad (10)$$

where ρ_C denotes the maximally mixed initial state of the cluster. The single-spin coherence contribution of the i th nucleus is denoted by $L_i(2\tau)$, while the pair-cluster coherence of nuclei (i, j) is denoted by $L_{ij}(2\tau)$. To avoid double counting of independent single-spin dynamics, the irreducible pair contribution is defined as

$$\tilde{L}_{ij}(2\tau) = \frac{L_{ij}(2\tau)}{L_i(2\tau)L_j(2\tau)}. \quad (11)$$

The total coherence within the CCE-2 approximation is then given by

$$L(2\tau) = \prod_i L_i(2\tau) \prod_{i < j} \tilde{L}_{ij}(2\tau). \quad (12)$$

Electron spin-echo simulation: The Hamiltonian of the three spin system consisting of the NV electron spin, ^{14}N nuclear spin, and a ^{13}C nuclear spin is given by \mathcal{H}_2 (Eq. 2). The Hamiltonian corresponding to the microwave field can be written as

$$\mathcal{H}_{\text{mw}}(t) = \gamma_e B_{\text{mw}} (\cos \eta S_x + \sin \eta S_y) \cos(\omega t + \varphi), \quad (13)$$

where η is the angle between the directions of the static and microwave magnetic fields in the transverse plane. B_{mw} , ω , and φ represent the amplitude, frequency, and phase of the microwave field respectively.

The unitary operator corresponding to the microwave pulses of the spin-echo sequence can be represented as

$$U_p = \mathcal{T} \exp \left(-i \int_0^t (\mathcal{H}_2 + \mathcal{H}_{\text{mw}}(t')) dt' \right), \quad (14)$$

where \mathcal{T} is the Dyson time-ordering operator and t is the duration of the pulse. The unitary operator is evaluated by discretizing the pulse duration t into N intervals of duration $\Delta t = \frac{t}{N}$. Here N is chosen such that $\Delta t \ll$

$\frac{1}{\|\mathcal{H}_2\|}$. So, the unitary operator can be approximated as

$$U_p \approx U_N U_{N-1} \cdots U_n \cdots U_2 U_1, \quad (15)$$

where

$$U_n = \exp \left(-i \int_{(n-1)\Delta t}^{n\Delta t} (\mathcal{H}_2 + \mathcal{H}_{\text{mw}}(t')) dt' \right). \quad (16)$$

The unitary operator corresponding to the free-evolution time τ can simply be written as

$$U_\tau = \exp(-i\mathcal{H}_2\tau). \quad (17)$$

The electron spin is initialized into the $|0\rangle$ state, and the ^{14}N and ^{13}C nuclear spins are in thermal equilibrium states, which are close to maximally mixed states. The corresponding initial density matrix of the spin system can be written as $\rho_i = |0\rangle\langle 0| \otimes \frac{1}{3} \mathbb{1}_3 \otimes \frac{1}{2} \mathbb{1}_2$, where $\mathbb{1}_2$ and $\mathbb{1}_3$ represent 2×2 and 3×3 identity matrices respectively. The final density matrix of the system after applying the spin-echo pulse sequence is

$$\rho_f = U_{\pi/2} U_\tau U_\pi U_\tau U_{\pi/2} (\rho_i) U_{\pi/2}^\dagger U_\tau^\dagger U_\pi^\dagger U_\tau^\dagger U_{\pi/2}^\dagger, \quad (18)$$

where $U_{\pi/2}$ and U_π represent unitary operators of $\pi/2$ and π pulses respectively. The population of the electron spin $|0\rangle$ state is calculated by using the expression

$$P_{|0\rangle} = \text{tr}(\rho_f |0\rangle\langle 0|). \quad (19)$$

The time-domain spin-echo signal is calculated as $\mathcal{S}(\tau) = P_{|0\rangle} \exp(-2\tau/T_2)$, where the exponential factor accounts for the decay of the signal. The spectrum is obtained by Fourier transforming $\mathcal{S}(\tau)$.

ACKNOWLEDGEMENTS

We thank T. S. Mahesh for the generous loan of one of the diamond samples used in this work. A.R. and R.K.K. acknowledge support from Department of Science & Technology - Science & Engineering Research Board (DST-SERB), India through grant no. SRG/2020/000765. S.D. thanks the Indian Institute of Technology, Madras, India, and the Science and Engineering Research Board (SERB Grant No. SRG/2023/000322), India, for start-up funding. S.D. and B.M. acknowledge the use of the computational facilities supported by a grant from the Mphasis F1 Foundation given to the Center for Quantum Information, Communication, and Computing (CQuICC).

AUTHOR CONTRIBUTIONS

R.K.K. designed the experiments. A.R. and P.L. performed the experiments. S.D. and R.K.K. developed the

interpretation of the experimental results. B.M., D.S., S.D. and R.K.K performed theoretical calculations and

simulations. R.K.K wrote the manuscript with contributions from D.S. and S.D. All authors discussed the results and commented on the manuscript.

-
- [1] W. H. Zurek, Decoherence and the transition from quantum to classical, *Physics Today* **44**, 36 (1991).
- [2] J. P. Dowling and G. J. Milburn, Quantum technology: The second quantum revolution, *Philosophical Transactions of the Royal Society A: Mathematical, Physical and Engineering Sciences* **361**, 1655 (2003).
- [3] D. Loss and D. P. DiVincenzo, Quantum computation with quantum dots, *Physical Review A* **57**, 120 (1998).
- [4] D. P. DiVincenzo, The physical implementation of quantum computation, *Fortschritte der Physik* **48**, 771 (2000).
- [5] H.-J. Briegel, W. Dür, J. I. Cirac, and P. Zoller, Quantum repeaters: The role of imperfect local operations in quantum communication, *Physical Review Letters* **81**, 5932 (1998).
- [6] A. I. Lvovsky, B. C. Sanders, and W. Tittel, Optical quantum memory, *Nature Photonics* **3**, 706 (2009).
- [7] C. L. Degen, F. Reinhard, and P. Cappellaro, Quantum sensing, *Rev. Mod. Phys.* **89**, 035002 (2017).
- [8] J. F. Barry, J. M. Schloss, E. Bauch, M. J. Turner, C. A. Hart, L. M. Pham, and R. L. Walsworth, Sensitivity optimization for nv-diamond magnetometry, *Rev. Mod. Phys.* **92**, 015004 (2020).
- [9] R. Schirhagl, K. Chang, M. Loretz, and C. L. Degen, Nitrogen-vacancy centers in diamond: Nanoscale sensors for physics and biology, *Annual Review of Physical Chemistry* **65**, 83 (2014).
- [10] J. Rovny, S. Gopalakrishnan, A. C. B. Jayich, P. Maletinsky, E. Demler, and N. P. de Leon, Nanoscale diamond quantum sensors for many-body physics, *Nature Reviews Physics* **6**, 753 (2024).
- [11] R. Katsumi, K. Takada, F. Jelezko, and T. Yatsui, Recent progress in hybrid diamond photonics for quantum information processing and sensing, *Communications Engineering* **4**, 85 (2025).
- [12] H. Park, J. Lee, H.-T. Lim, H. Shin, D. Kim, J. Kim, X. Kong, and S.-Y. Lee, Decoherence of nitrogen-vacancy spin ensembles in a nitrogen electron-nuclear spin bath in diamond, *npj Quantum Information* **8**, 95 (2022).
- [13] N. Zhao, S.-W. Ho, and R.-B. Liu, Decoherence and dynamical decoupling control of nitrogen-vacancy center electron spins in nuclear spin baths, *Physical Review B* **85**, 115303 (2012).
- [14] G. de Lange, Z. H. Wang, D. Ristè, V. V. Dobrovitski, and R. Hanson, Universal dynamical decoupling of a single solid-state spin from a spin bath, *Science* **330**, 60 (2010).
- [15] D. Suter and G. A. Álvarez, Colloquium: Protecting quantum information against environmental noise, *Reviews of Modern Physics* **88**, 041001 (2016).
- [16] J. R. Maze, J. M. Taylor, and M. D. Lukin, Electron spin decoherence of single nitrogen-vacancy defects in diamond, *Phys. Rev. B* **78**, 094303 (2008).
- [17] P. L. Stanwix, L. M. Pham, J. R. Maze, D. Le Sage, T. K. Yeung, P. Cappellaro, P. R. Hemmer, A. Yacoby, M. D. Lukin, and R. L. Walsworth, Coherence of nitrogen-vacancy electronic spin ensembles in diamond, *Phys. Rev. B* **82**, 201201 (2010).
- [18] C. S. Shin, C. E. Avalos, M. C. Butler, H.-J. Wang, S. J. Seltzer, R.-B. Liu, A. Pines, and V. S. Bajaj, Suppression of electron spin decoherence of the diamond nv center by a transverse magnetic field, *Phys. Rev. B* **88**, 161412 (2013).
- [19] E. L. Hahn, Spin echoes, *Physical Review* **80**, 580 (1950).
- [20] L. Childress, M. V. Gurudev Dutt, J. M. Taylor, A. S. Zibrov, F. Jelezko, J. Wrachtrup, P. R. Hemmer, and M. D. Lukin, Coherent dynamics of coupled electron and nuclear spin qubits in diamond, *Science* **314**, 281 (2006).
- [21] P. Lamba, A. Rana, S. Halder, S. Dhomkar, D. Suter, and R. K. Kamineni, Vector detection of ac magnetic fields by nitrogen vacancy centers of single orientation in diamond, *Phys. Rev. B* **109**, 195424 (2024).
- [22] A. Rana, P. Lamba, A. Ghosh, S. Dhomkar, and R. K. Kamineni, Imaging of microwave magnetic field orientation using continuous-wave experiments on nitrogen-vacancy centers in diamond, *Journal of Physics D: Applied Physics* **58**, 435302 (2025).
- [23] E. Moreva, E. Bernardi, P. Traina, A. Sosso, S. D. Tchernij, J. Forneris, F. Picollo, G. Brida, i. c. v. Pastuović, I. P. Degiovanni, P. Olivero, and M. Genovese, Practical applications of quantum sensing: A simple method to enhance the sensitivity of nitrogen-vacancy-based temperature sensors, *Phys. Rev. Appl.* **13**, 054057 (2020).
- [24] Z. Qiu, U. Vool, A. Hamo, and A. Yacoby, Nuclear spin assisted magnetic field angle sensing, *npj Quantum Information* **7**, 39 (2021).
- [25] E. Fraval, M. J. Sellars, and J. J. Longdell, Method of extending hyperfine coherence times in $\text{pr}^{3+}:\text{y}_2\text{si}_5\text{o}_5$, *Phys. Rev. Lett.* **92**, 077601 (2004).
- [26] M. Lovrić, P. Glasenapp, D. Suter, B. Tumino, A. Ferrier, P. Goldner, M. Sabooni, L. Rippe, and S. Kröll, Hyperfine characterization and spin coherence lifetime extension in $\text{pr}^{3+}:\text{la}_2(\text{wo}_4)_3$, *Phys. Rev. B* **84**, 104417 (2011).
- [27] K. R. K. Rao and D. Suter, Level anti-crossings of a nitrogen-vacancy center in diamond: decoherence-free subspaces and 3d sensors of microwave magnetic fields, *New Journal of Physics* **22**, 103065 (2020).
- [28] B. Mistri, S. Mahajan, F. Donaldson, R. K. Kamineni, and S. Dhomkar, Identifying optimal magnetic field configurations for decoherence mitigation of boron vacancies in hexagonal boron nitride, *Phys. Rev. B* **112**, 245141 (2025).
- [29] W. M. Witzel and S. Das Sarma, Quantum theory for electron spin decoherence induced by nuclear spin dynamics in semiconductor quantum computer architectures: Spectral diffusion of localized electron spins in the nuclear solid-state environment, *Phys. Rev. B* **74**, 035322 (2006).
- [30] W. Yang and R.-B. Liu, Quantum many-body theory of qubit decoherence in a finite-size spin bath, *Phys. Rev. B* **78**, 085315 (2008).
- [31] W. B. Mims, Envelope modulation in spin-echo experiments, *Phys. Rev. B* **5**, 2409 (1972).

- [32] A. Jarmola, I. Fescenko, V. M. Acosta, M. W. Doherty, F. K. Fatemi, T. Ivanov, D. Budker, and V. S. Malinovsky, Robust optical readout and characterization of nuclear spin transitions in nitrogen-vacancy ensembles in diamond, [Phys. Rev. Res. **2**, 023094 \(2020\)](#).
- [33] S. Lourette, A. Jarmola, V. M. Acosta, A. G. Birdwell, D. Budker, M. W. Doherty, T. Ivanov, and V. S. Malinovsky, Temperature sensitivity of ^{14}N - v and ^{15}N - v ground-state manifolds, [Phys. Rev. Appl. **19**, 064084 \(2023\)](#).
- [34] M. Liu, X. Zhao, T. Xie, S. Xu, F. Shi, and C.-K. Duan, First-principles investigation of the impact of stress and lattice vibration on the hyperfine interactions of the nitrogen-vacancy center in diamond, [Phys. Rev. B **108**, 155150 \(2023\)](#).

Supplementary Information: Spin bath mediated long-lived coherent oscillations of NV centers in diamond

S1 T_2 for different θ values

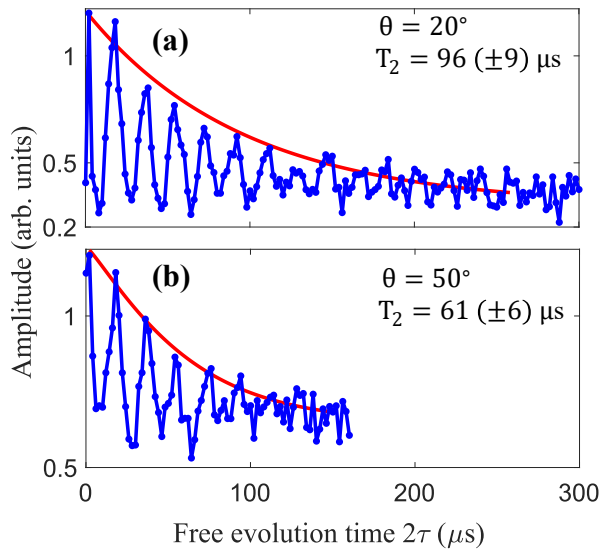


Figure 1: Spin-echo signals of ensemble NV centers measured in a static magnetic field of 10.7 mT oriented at (a) 20° and (b) 50° with respect to the NV-axis. Red curves correspond to the decay of the echo revivals fit to the equation $a \exp(-2\tau/T_2)^n + b$. The revival frequency is equal to $\frac{1}{2}\gamma_C B$. Errors in T_2 correspond to one standard deviation confidence intervals obtained from the fit.

It has been demonstrated in Ref. [1] that the spin-echo coherence time (T_2) of NV centers decreases as the angle (θ) between the NV axis and the static magnetic field increases. We also observe this experimentally as shown in Fig. 1. At $\theta = 20^\circ$, $T_2 = 96 (\pm 9) \mu\text{s}$ and at $\theta = 50^\circ$, $T_2 = 61 (\pm 6) \mu\text{s}$, which are much smaller compared to $T_2 = 208 \mu\text{s}$ at $\theta = 0^\circ$. T_2 continues to decrease till around $\theta = 84^\circ$. However, from $\theta = 85^\circ$ to 90° , T_2 increases again as shown in Fig. 2 of the main text.

S2 Energy level diagram of the NV center in a transverse magnetic field

The energy level diagram of a three-spin system consisting of the NV electron, ^{14}N nucleus and a bath ^{13}C nucleus, relevant for the electron spin transition $|0\rangle \leftrightarrow |-\rangle$, in a transverse magnetic field of 10.7 mT is shown in Fig. 2. The spin states are arranged in the order $|e^-, ^{14}\text{N}, ^{13}\text{C}\rangle$. The eigenstates of the ^{14}N nuclear spin depend on the ^{13}C nuclear spin hyperfine coupling term $A_{zx}^C S_z I_x$. If $A_{zx}^C = 0$, the ^{14}N nuclear spin eigenstates are $|0\rangle$ and $|\pm\rangle$ for both the $|0\rangle$ and $|-\rangle$ subspaces of the electron spin. However, for $A_{zx}^C \neq 0$, the ^{14}N eigenstates are $|0\rangle$ and $|\pm\rangle$ if the electron spin is in the $|0\rangle$ state, and they are $|0\rangle$

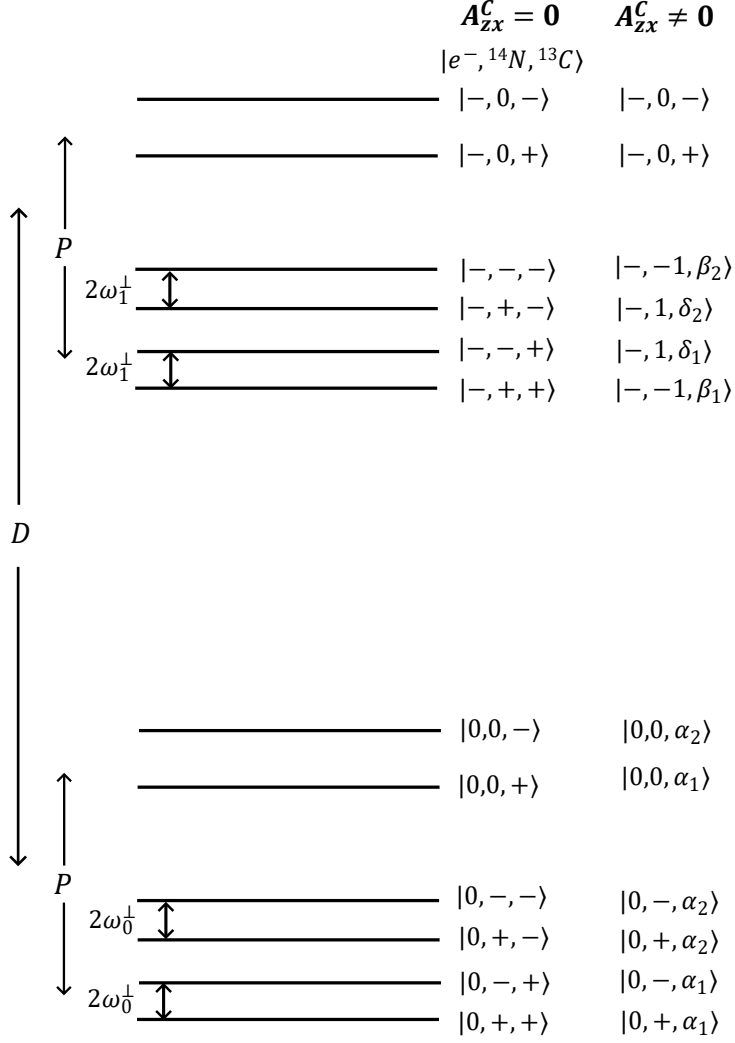


Figure 2: Energy level diagram corresponding to the $|0\rangle$ and $|-\rangle$ states of the NV electron spin coupled to the ${}^{14}\text{N}$ nuclear spin and a ${}^{13}\text{C}$ nuclear spin, in a transverse magnetic field of 10.7 mT. The eigenstates are given for both without and with the ${}^{13}\text{C}$ hyperfine coupling term $A_{zx}^C S_z I_x$ in the Hamiltonian. For the electron and ${}^{14}\text{N}$ nuclear spins $|\pm\rangle = \frac{|-1\rangle \pm |1\rangle}{\sqrt{2}}$ and for the ${}^{13}\text{C}$ $|\pm\rangle = \frac{1}{\sqrt{2}} (|-\frac{1}{2}\rangle \pm |\frac{1}{2}\rangle)$. For $A_{zx}^C = 0.25$ MHz, $|\alpha_1\rangle \approx 0.81|\frac{1}{2}\rangle + 0.58|-\frac{1}{2}\rangle$, $|\beta_1\rangle \approx 0.74|\frac{1}{2}\rangle + 0.66|-\frac{1}{2}\rangle$, $|\delta_1\rangle \approx 0.63|\frac{1}{2}\rangle + 0.78|-\frac{1}{2}\rangle$. $|\alpha_2\rangle$, $|\beta_2\rangle$, and $|\delta_2\rangle$ are states orthogonal to $|\alpha_1\rangle$, $|\beta_1\rangle$, and $|\delta_1\rangle$ respectively.

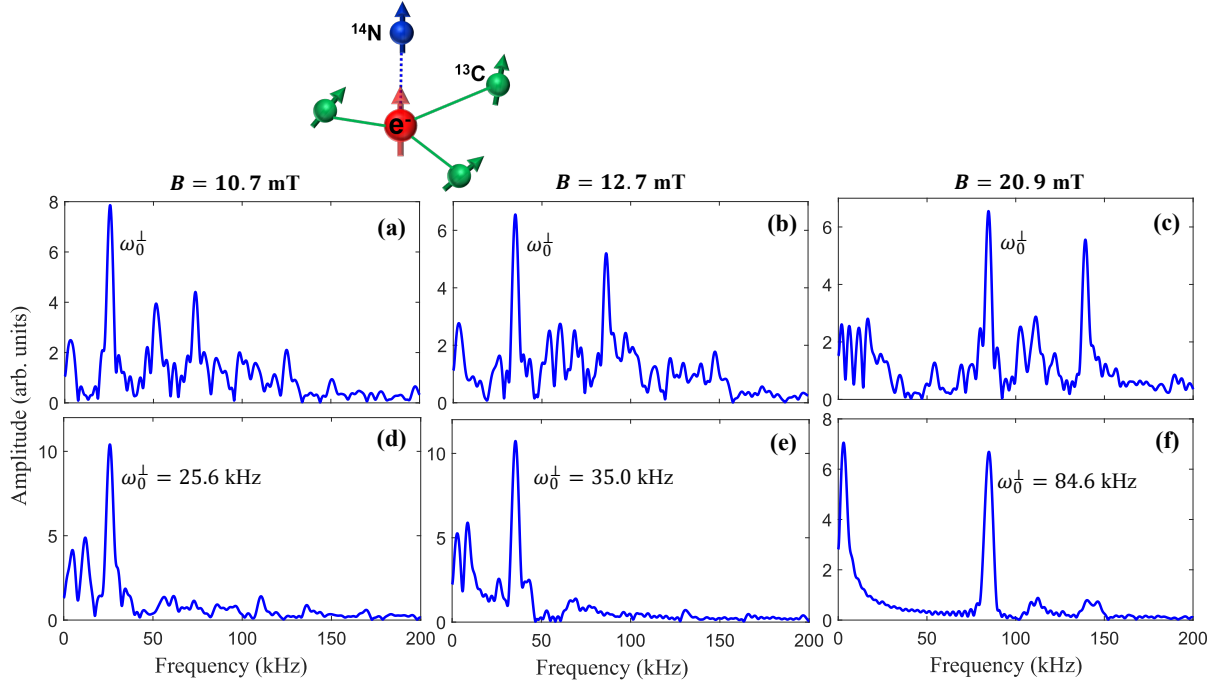


Figure 3: Fourier transforms of the simulated electron spin-echo signals of a five-spin system (NV electron spin, ^{14}N nuclear spin, and three ^{13}C nuclear spins) for three different amplitudes of the transverse magnetic field and two different sets of ^{13}C hyperfine tensors. (a), (b) and (c) are simulated using the hyperfine tensors (expressed in MHz) of Eq. 1, and (d), (e) and (f) are simulated using those of Eq. 2.

and $|\pm 1\rangle$ if the electron spin is in the $|-\rangle$ state. That is, the ^{14}N nuclear spin state is conditioned on the electron spin state because of the hyperfine coupling of the ^{13}C nuclear spin.

S3 Simulation of electron spin-echo for a 5-spin system

In the main text, electron spin-echo simulations of a 3-spin system consisting of the NV electron spin, the ^{14}N nuclear spin, and a ^{13}C nuclear spin are shown. Here, in Fig. 3, we show the results of simulations performed on a 5-spin system comprising an NV center coupled to three ^{13}C nuclear spins. Spectra shown in Figs. 3(a)–(c) are simulated using the ^{13}C hyperfine tensors (expressed in MHz) given in Eq. 1, for the transverse field strengths 10.7 mT, 12.7 mT, and 20.9 mT, respectively. Those shown in Figs. 3(d)–(f) are simulated using the tensors in Eq. 2 for the same fields. The spectra show several peaks. However, the most prominent of them is the peak at the frequency ω_0^\perp , which corresponds to the ^{14}N transition $|+\rangle \leftrightarrow |-\rangle$ within the $|0\rangle$ subspace of the electron spin. This peak appears in the spectrum if there is at least one ^{13}C nuclear spin coupled to the electron spin with the hyperfine parameter A_{zx}^C having a value of 10 kHz or higher. It is independent of the values of the other hyperfine parameters or the number of ^{13}C nuclear spins coupled. The frequencies and amplitudes of other peaks seen in the spectra depend on the ^{13}C hyperfine coupling strengths. As shown in Fig. 3, the frequency ω_0^\perp increases non-linearly with the magnetic field strength, and its values observed in the 5-spin simulations match very well with those in the 3-spin simulation and the experimental spin-echo envelope modulation frequencies shown in Fig. 3 of the main text.

$$\mathbf{A}_1^C = \begin{pmatrix} -0.063 & -0.223 & 0.461 \\ -0.223 & -0.320 & -0.266 \\ 0.461 & -0.266 & 0.611 \end{pmatrix}, \mathbf{A}_2^C = \begin{pmatrix} 0.620 & -0.028 & 0.280 \\ -0.028 & 0.442 & 0.097 \\ 0.280 & 0.097 & 0.314 \end{pmatrix}, \mathbf{A}_3^C = \begin{pmatrix} 0.039 & -0.020 & 0.140 \\ -0.020 & -0.059 & -0.027 \\ 0.140 & -0.027 & 0.113 \end{pmatrix}. \quad (1)$$

$$\mathbf{A}_1^C = \begin{pmatrix} -0.028 & -0.014 & -0.112 \\ -0.014 & -0.106 & 0.015 \\ -0.112 & 0.015 & 0.052 \end{pmatrix}, \mathbf{A}_2^C = \begin{pmatrix} 0.078 & 0.059 & -0.013 \\ 0.059 & -0.052 & -0.004 \\ -0.013 & -0.004 & -0.094 \end{pmatrix}, \mathbf{A}_3^C = \begin{pmatrix} 0.510 & 0.090 & -0.056 \\ 0.090 & 0.551 & -0.291 \\ -0.056 & -0.291 & 0.314 \end{pmatrix}. \quad (2)$$

S4 Gradient and Curvature Calculations

The spin Hamiltonian is

$$H = DS_z^2 + \gamma_e B_x S_x + \gamma_e B_y S_y + \gamma_e B_z S_z + \gamma_e (b_x S_x + b_y S_y + b_z S_z), \quad (3)$$

where $\vec{b} = (b_x, b_y, b_z)$ denotes the fluctuating magnetic field. Defining the total magnetic field components

$$\bar{B}_x = B_x + b_x, \quad \bar{B}_y = B_y + b_y, \quad \bar{B}_z = B_z + b_z, \quad (4)$$

the Hamiltonian becomes

$$H = DS_z^2 + \gamma_e \bar{B}_x S_x + \gamma_e \bar{B}_y S_y + \gamma_e \bar{B}_z S_z. \quad (5)$$

In the $\{|+1\rangle, |0\rangle, |-1\rangle\}$ basis, the Hamiltonian matrix reads

$$H = \begin{pmatrix} D + \gamma_e \bar{B}_z & \frac{\gamma_e}{\sqrt{2}}(\bar{B}_x - i\bar{B}_y) & 0 \\ \frac{\gamma_e}{\sqrt{2}}(\bar{B}_x + i\bar{B}_y) & 0 & \frac{\gamma_e}{\sqrt{2}}(\bar{B}_x - i\bar{B}_y) \\ 0 & \frac{\gamma_e}{\sqrt{2}}(\bar{B}_x + i\bar{B}_y) & D - \gamma_e \bar{B}_z \end{pmatrix}. \quad (6)$$

We define

$$C = \frac{\gamma_e}{\sqrt{2}}(\bar{B}_x - i\bar{B}_y), \quad (7)$$

$$C^* = \frac{\gamma_e}{\sqrt{2}}(\bar{B}_x + i\bar{B}_y), \quad (8)$$

$$K = \gamma_e \bar{B}_z, \quad (9)$$

so that

$$|C|^2 = CC^* = \frac{\gamma_e^2}{2}(\bar{B}_x^2 + \bar{B}_y^2). \quad (10)$$

The characteristic polynomial is

$$P(E) = \det(H - EI) = \begin{vmatrix} D + K - E & C & 0 \\ C^* & -E & C \\ 0 & C^* & D - K - E \end{vmatrix}. \quad (11)$$

Evaluating the determinant gives the cubic equation

$$E^3 - 2DE^2 + (D^2 - \gamma_e^2 B^2)E + D\gamma_e^2 B_\perp^2 = 0, \quad (12)$$

where $B^2 = \bar{B}_x^2 + \bar{B}_y^2 + \bar{B}_z^2$, $B_\perp^2 = \bar{B}_x^2 + \bar{B}_y^2$.

S4.1 Depressed Cubic Form

Using the substitution

$$E = E' + \frac{2D}{3}, \quad (13)$$

the cubic reduces to the depressed form

$$E'^3 + pE' + q = 0, \quad (14)$$

with

$$p = -\frac{D^2}{3} - \gamma_e^2 B^2, \quad (15)$$

$$q = \frac{2D^3}{27} - \frac{2D\gamma_e^2 B^2}{3} + D\gamma_e^2 B_\perp^2. \quad (16)$$

S4.2 Eigenvalues

Since the Hamiltonian is Hermitian, all eigenvalues are real. For $p < 0$, they can be written as

$$E_k = \frac{2D}{3} + 2\sqrt{-\frac{p}{3}} \cos\left(\phi + \frac{2\pi k}{3}\right), \quad (17)$$

where

$$\phi = \frac{1}{3} \cos^{-1}\left(\frac{3q}{2p} \sqrt{-\frac{3}{p}}\right), \quad k = 0, 1, 2. \quad (18)$$

The ground-state energy E_g is obtained by selecting the minimum of the three real roots in Eq. (15). For $p < 0$, the ordering of the cosine terms is fixed by

$$\cos\left(\phi + \frac{4\pi}{3}\right) \leq \cos\left(\phi + \frac{2\pi}{3}\right) \leq \cos(\phi), \quad 0 \leq \phi \leq \frac{\pi}{3},$$

which implies

$$\boxed{E_g = \frac{2D}{3} + 2\sqrt{-\frac{p}{3}} \cos\left(\phi + \frac{4\pi}{3}\right), \quad k = 2} \quad (19)$$

The remaining two roots correspond to the first and second excited states, respectively.

S4.3 Gradient of the Transition Energy

The sensitivity of a spin transition to magnetic-field fluctuations is quantified by the gradient of the transition energy with respect to the magnetic field. For an arbitrary magnetic field orientation we define the transition energy

$$f_i = E_{ei} - E_g, \quad (20)$$

where E_g and E_{ei} ($i = 1, 2$) denote the ground and excited eigenenergies, respectively.

The eigenenergies are the real roots of the cubic equation

$$P(E, \vec{B}) = E^3 - 2DE^2 + (D^2 - \gamma^2 B^2)E + D\gamma^2 B_\perp^2 = 0, \quad (21)$$

Using implicit differentiation of Eq. (21), the gradient of an individual eigenenergy is

$$\frac{\partial E_k}{\partial b_\alpha} = - \left. \frac{\partial P / \partial b_\alpha}{\partial P / \partial E} \right|_{E=E_k}, \quad (22)$$

where

$$\Lambda_k \equiv \left. \frac{\partial P}{\partial E} \right|_{E_k} = 3E_k^2 - 4DE_k + (D^2 - \gamma^2 B^2). \quad (23)$$

Evaluating the derivatives explicitly yields

$$\frac{\partial E_k}{\partial b_x} = - \frac{2\gamma^2 \bar{B}_x (D - E_k)}{\Lambda_k}, \quad (24)$$

$$\frac{\partial E_k}{\partial b_y} = - \frac{2\gamma^2 \bar{B}_y (D - E_k)}{\Lambda_k}, \quad (25)$$

$$\frac{\partial E_k}{\partial b_z} = \frac{2\gamma^2 \bar{B}_z E_k}{\Lambda_k}. \quad (26)$$

The gradient of the transition energy follows directly as

$$\vec{\nabla}_{\mathbf{b}} f_i = \vec{\nabla}_{\mathbf{b}} E_{ei} - \vec{\nabla}_{\mathbf{b}} E_g. \quad (27)$$

To obtain a scalar, orientation-independent measure of first-order magnetic-field sensitivity, we define the gradient magnitude

$$\mathcal{G}_i = \left| \vec{\nabla}_{\mathbf{b}} f_i \right| = \sqrt{\sum_{\alpha=x,y,z} \left(\frac{\partial f_i}{\partial b_\alpha} \right)^2}. \quad (28)$$

Vanishing \mathcal{G}_i identifies clock or near-clock transitions that are first-order insensitive to magnetic noise.

Evaluating $\frac{\partial f_i}{\partial b_\alpha}$ and substituting them in Eq. 28, leads to

$$\mathcal{G}_i = \left| \vec{\nabla}_{\mathbf{b}} f_i \right| = 2\gamma_e^2 \sqrt{(\bar{B}_x^2 + \bar{B}_y^2) \left[\frac{(D - E_g)}{\Lambda_g} - \frac{(D - E_{ei})}{\Lambda_{ei}} \right]^2 + \bar{B}_z^2 \left[\frac{E_{ei}}{\Lambda_{ei}} - \frac{E_g}{\Lambda_g} \right]^2}. \quad (29)$$

Parallel field:

$B_x = B_y = 0$, $B_z = B$. The gradient becomes

$$\left| \vec{\nabla}_{\mathbf{b}} f_i \right| = 2\gamma_e^2 \sqrt{(b_x^2 + b_y^2) \left[\frac{(D - E_g)}{\Lambda_g} - \frac{(D - E_{ei})}{\Lambda_{ei}} \right]^2 + \bar{B}_z^2 \left[\frac{E_{ei}}{\Lambda_{ei}} - \frac{E_g}{\Lambda_g} \right]^2}, \quad (30)$$

where $D - E_g = D$ and $D - E_{ei} = \pm\gamma_e B$. Under the approximation $\gamma_e b \ll \gamma_e B \ll D$, $\Lambda_g \approx D^2$ and $\Lambda_{ei} \approx \pm 2D\gamma_e B$. Substituting them in Eq. 30 and simplifying, we get

$$\left| \vec{\nabla}_{\mathbf{b}} f_i \right| \approx \gamma_e. \quad (31)$$

Transverse field:

$B_y = B_z = 0$, $B_x = B$. The gradient becomes

$$\left| \vec{\nabla}_{\mathbf{b}} f_i \right| = 2\gamma_e^2 \sqrt{(\bar{B}_x^2 + b_y^2) \left[\frac{(D - E_g)}{\Lambda_g} - \frac{(D - E_{ei})}{\Lambda_{ei}} \right]^2 + b_z^2 \left[\frac{E_{ei}}{\Lambda_{ei}} - \frac{E_g}{\Lambda_g} \right]^2}, \quad (32)$$

Under the approximation $\gamma_e b \ll \gamma_e B \ll D$, $E_g \approx 0$, $E_{ei} \approx D$, $\Lambda_g \approx D^2$, and $\Lambda_{ei} \approx -\gamma_e^2 B^2$. Substituting them in Eq. 32 and simplifying, we get

$$\left| \vec{\nabla}_{\mathbf{b}} f_i \right| \approx 2\gamma_e^2 B/D. \quad (33)$$

S4.4 Curvature of the Transition Energy

When the first-order magnetic-field sensitivity is suppressed, the dominant contribution to decoherence arises from second-order field fluctuations. This effect is quantified by the curvature of the transition energy with respect to the magnetic field.

Starting again from the implicit eigenvalue condition $P(E_k, \vec{B}) = 0$, a second differentiation with respect to a field component b_α gives

$$\frac{\partial^2 E_k}{\partial b_\alpha^2} = -\frac{1}{\Lambda_k} \left[\frac{\partial^2 P}{\partial b_\alpha^2} + 2 \frac{\partial^2 P}{\partial E \partial b_\alpha} \frac{\partial E_k}{\partial b_\alpha} + \frac{\partial^2 P}{\partial E^2} \left(\frac{\partial E_k}{\partial b_\alpha} \right)^2 \right]_{E=E_k}. \quad (34)$$

The required derivatives of $P(E, \vec{B})$ are

$$\frac{\partial^2 P}{\partial b_x^2} = 2\gamma^2(D - E), \quad (35)$$

$$\frac{\partial^2 P}{\partial b_y^2} = 2\gamma^2(D - E), \quad (36)$$

$$\frac{\partial^2 P}{\partial b_z^2} = -2\gamma^2 E, \quad (37)$$

$$\frac{\partial^2 P}{\partial E \partial b_\alpha} = -2\gamma^2 b_\alpha, \quad (38)$$

$$\frac{\partial^2 P}{\partial E^2} = 6E - 4D. \quad (39)$$

Substituting these expressions into Eq. 34 yields closed-form analytical expressions for $\partial^2 E_k / \partial b_\alpha^2$ for all field orientations. The curvature of the transition energy is then

$$\frac{\partial^2 f_i}{\partial b_\alpha^2} = \frac{\partial^2 E_{ei}}{\partial b_\alpha^2} - \frac{\partial^2 E_g}{\partial b_\alpha^2}. \quad (40)$$

We define an orientation-independent curvature metric as

$$\mathcal{C}_i = \sqrt{\sum_{\alpha=x,y,z} \left(\frac{\partial^2 f_i}{\partial b_\alpha^2} \right)^2}. \quad (41)$$

The quantity \mathcal{C}_i characterizes the residual second-order magnetic sensitivity of the transition energy, where $\mathcal{G}_i \approx 0$.

References

- [1] P. L. Stanwix, L. M. Pham, J. R. Maze, D. Le Sage, T. K. Yeung, P. Cappellaro, P. R. Hemmer, A. Yacoby, M. D. Lukin and R. L. Walsworth, *Phys. Rev. B*, 2010, **82**, 201201.